Low-energy Compton scattering in materials

Rouven Essig,[1] Yonit Hochberg,[2] Yutaro Shoji,[2,3] Aman Singal⬤,[1] and Gregory Suczewski[1]

[1]*C.N. Yang Institute for Theoretical Physics, Stony Brook University, Stony Brook, New York 11794, USA*
[2]*Racah Institute of Physics, Hebrew University of Jerusalem, Jerusalem 91904, Israel*
[3]*Jožef Stefan Institute, Jamova 39, 1000 Ljubljana, Slovenia*

Low-energy Compton scattering is an important background for sub-GeV dark matter direct-detection and other experiments. Current Compton scattering calculations typically rely on assumptions that are not valid in the low-energy region of interest, beneath ~50 eV. Here we relate the low-energy Compton scattering differential cross section to the dielectric response of the material. Our new approach can be used for a wide range of materials and includes all-electron, band-structure, and collective effects, which can be particularly relevant at low energies. We demonstrate the strength of our approach in several solid-state systems, in particular, Si, Ge, GaAs, and SiC, which are relevant for current and proposed experiments searching for dark matter, neutrinos, and millicharged particles.

I. INTRODUCTION

Tremendous progress has been made in dark matter (DM) direct-detection experiments in the last decade. Although several direct-detection experiments are now searching for DM with sub-GeV masses through their interactions with electrons (see, e.g., Ref. [1] and references therein), this mass region remains to be fully explored. A crucial ingredient of direct-detection searches for DM is a detailed understanding of backgrounds. It is especially important to understand backgrounds that lie in the ~1–50 eV energy range since the relevant energy transfer in a collision between a sub-GeV DM particle and electrons in, e.g., semiconductors is typically a few eV, decaying rapidly for higher energies [2].

Environmental photons that Compton scatter off detector electrons can produce low-energy ionization events and thus constitute an important background in experiments searching for sub-GeV DM. It is therefore imperative to have reliable calculations of the Compton scattering cross section and spectrum down to the lowest energies probed by an experiment. The differential Compton scattering cross section at low energies is most commonly calculated using the relativistic impulse approximation (RIA). The RIA is implemented in many computational software programs, including Geant4 [3–5]. The FEFF program [6–9] improves on the RIA and was found in Ref. [10] to agree better than RIA

with data at energies $\gtrsim 100$ eV. However, RIA does not incorporate band-structure effects, while FEFF includes these effects only through the Korringa-Kohn-Rostoker Green function method [11,12] and a "muffin-tin" potential. Moreover, both RIA and FEFF assume the photon interacts with a single electron and neglect collective effects of the electron density. These assumptions are typically not valid at energies below $\mathcal{O}(50 \text{ eV})$ (depending on the material) where only valence electrons can be excited.

In this work, we develop a new approach for calculating the Compton scattering cross section in the low-energy regime. In particular, we relate the differential Compton cross section to the response of the material via the dielectric function of the target. This allows us to relate the Compton rate to directly measurable properties of a detector. The dielectric function formalism contains the full material response, including the band-structure and many-body effects, and can be calculated using existing codes and analytical models, or, in principle, obtained from data. As we will see, the full response of the material is indeed important for low-energy Compton scattering and is crucial in at least some of the materials we consider.

Our results will enable a better understanding of the expected Compton-scattering backgrounds in direct-detection experiments targeted at sub-GeV DM masses [1] and experiments searching for neutrino scattering at low energies [13], and they will help us distinguish them from potential beyond-the-Standard-Model signals. Our work can additionally be used to calibrate detectors for low-energy scattering events [10,14] and to probe our understanding of scattering with electrons bound in semiconductors.

This paper is organized as follows. Section II reviews the RIA method that is most commonly used for computing

low-energy Compton scattering. In Sec. III, we present our new approach for calculating the Compton scattering differential cross section in terms of the dielectric function, enhancing accuracy at low energies. Section IV presents our results for Compton scattering rates in various materials, with particular emphasis on silicon. We summarize in Sec. V. The Appendixes elaborate on single-electron excitations, give details of the density functional theory we use, and explain why the Lindhard model works well for our purposes.

II. RELATIVISTIC IMPULSE APPROXIMATION

The spin-averaged differential cross section for free-electron Compton scattering in the laboratory frame is well known [15],

$$\frac{d\sigma}{d\cos\theta} = \frac{\pi\alpha^2}{m^2}\left(\frac{\omega'}{\omega}\right)^2\left(\frac{\omega'}{\omega} + \frac{\omega}{\omega'} - \sin^2\theta\right), \qquad (1)$$

where ω is the initial photon energy, ω' is the final photon energy, m is the mass of the electron, α is the electromagnetic fine-structure constant, and θ is the angle between the initial and final photon directions. For electrons that are not free, the above Compton scattering cross section must be modified. The most common method of calculation is known as the relativistic impulse approximation, which assumes the photon scatters off of a single electron with a momentum distribution.

In the RIA formulation, the differential cross section can be factored into two pieces, one pertaining to the free-electron-photon interaction and the other, known as the Compton profile, capturing the many-electron effects (typically only for an isolated atom) via the momentum distribution of the electron [16–18]. It is convenient to define the momentum transfer vector, $\vec{q} = \vec{k'} - \vec{k} = \vec{p} - \vec{p'}$, where $\vec{k}$ ($\vec{p}$) and $\vec{k'}$ ($\vec{p'}$) are the initial and final momenta of
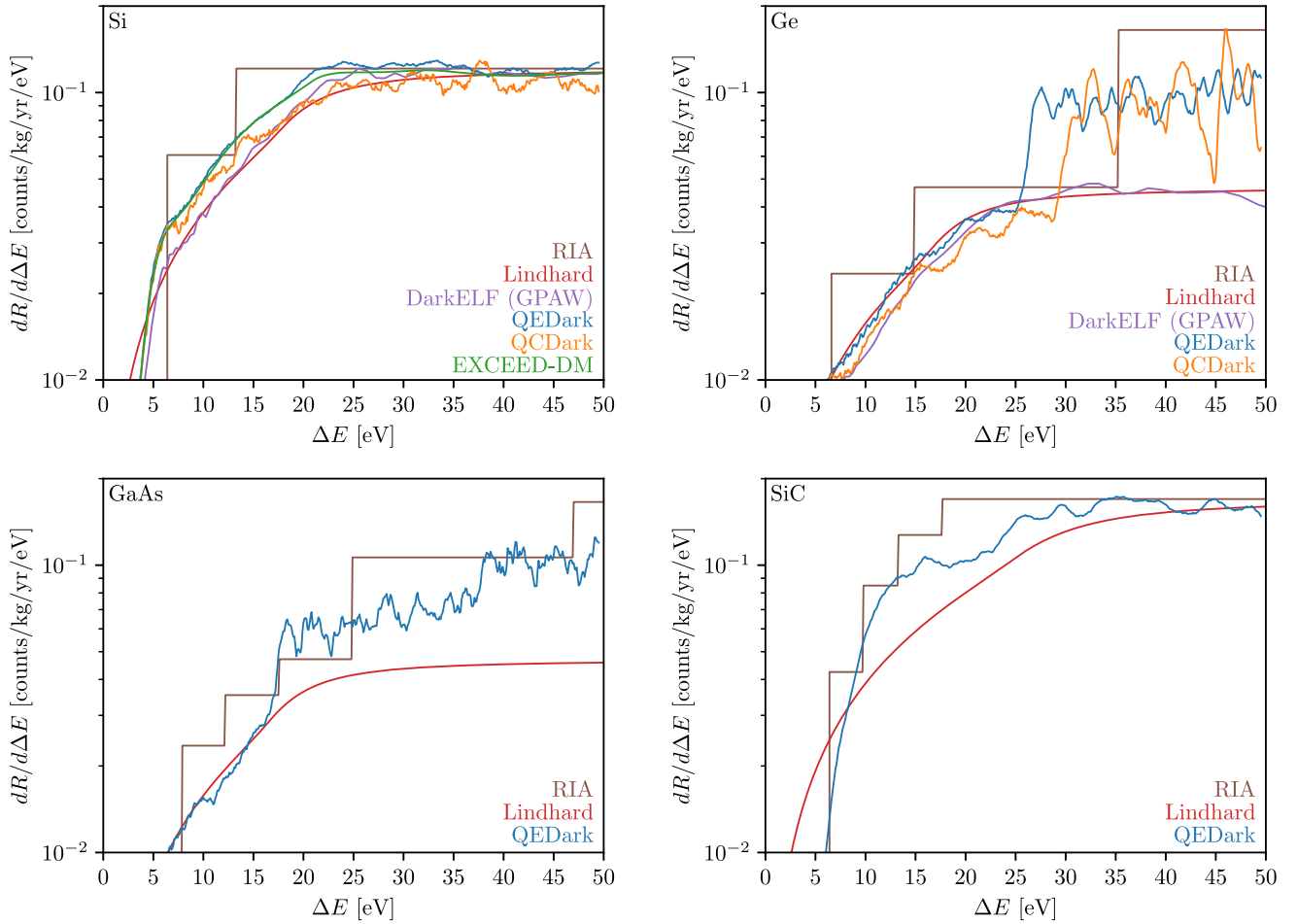
FIG. 1.   Compton scattering rates for incoming photons with $E_\gamma = 1.461$ MeV and $n_\gamma = 1.25 \times 10^{-14}$ cm^{-3}. The top-left panel shows the rates for Si, the top-right panel for Ge, the bottom-left panel for GaAs, and the bottom-right panel for SiC (3C) crystals. RIA is described in Sec. II and the Lindhard model in Eq. (20). For DarkELF, we use the GPAW results with local field effects from Refs. [21,22]. For QEDark [23] and QCDark [24], we use Eq. (23) to calculate the imaginary part of the dielectric function, and we use the real part of the Lindhard dielectric function when constructing the full material response. We use the available valence-to-conduction-only results from EXCEED-DM [25].

the electron (photon) in the laboratory frame. The energy of the electron is $E(k) = \sqrt{k^2 + m^2}$. Then, the differential cross section per unit cell is given by

$$\left(\frac{d^2\sigma}{d\omega' d\Omega'}\right)_{\text{RIA}} = N_{\text{atoms}} \frac{\alpha^2}{2qE(k_z)} \frac{\omega'}{\omega} \bar{X}(k_z) J(k_z). \quad (2)$$

Here, we have assumed the crystal is composed of a single element, and N_{atoms} is the number of atoms per cell. If there are multiple elements, the cross section is given by the sum of the contributions of each.

The Compton profile, $J(k_z)$, is defined as

$$J(k_z) = \int \rho(\vec{k}) dk_x dk_y, \quad (3)$$

where $\rho(\vec{k})$ is the ground-state electron-momentum density. The kernel function $\bar{X}$ is proportional to the squared-averaged amplitude for free-electron Compton scattering,

$$\bar{X}(k_z) = \frac{K_f(k_z)}{K_i(k_z)} + \frac{K_i(k_z)}{K_f(k_z)} + 2m^2 \left(\frac{1}{K_i(k_z)} - \frac{1}{K_f(k_z)}\right)$$
$$+ m^4 \left(\frac{1}{K_i(k_z)} - \frac{1}{K_f(k_z)}\right)^2, \quad (4)$$

evaluated at

$$k_z = -\frac{\vec{k} \cdot \vec{q}}{q}$$
$$= \frac{\omega\omega'(1 - \cos\theta) - E(k_z)(\omega - \omega')}{q}, \quad (5)$$

where

$$K_i(k_z) = E(k_z)\omega + \frac{\omega(\omega - \omega'\cos\theta)k_z}{q} \quad (6)$$

and

$$K_f(k_z) = K_i(k_z) - \omega\omega'(1 - \cos\theta). \quad (7)$$

To include the effect of the binding energy, we consider only the energetically allowed electrons in the Compton profile,

$$\bar{J}(p_z, \Delta E) = \sum_i \Theta(\Delta E - E_i) \int \rho_i(\vec{k}) dk_x dk_y, \quad (8)$$

where E_i and $\rho_i(\vec{k})$ are the ionization energy and the electron density of the ith electron. As the energy transfer exceeds the binding energy of the shells, more electrons become kinematically available to scatter, resulting in a sharp enhancement in the cross section and scattering rate.

TABLE I. Binding energies of valence electrons for isolated atoms computed with cFAC [20] ($\Delta E < 100$ eV). The corresponding orbitals are indicated together.

Atom	Binding energy (eV)		
C	$9.76[2p^2]$	$17.6[2s^2]$	$\cdots$
Si	$6.39[3p^2]$	$13.2[3s^2]$	$\cdots$
Ga	$5.32[4p^1]$	$12.1[4s^2]$	$24.8[3d^{10}]$
Ge	$6.54[4p^2]$	$14.8[4s^2]$	$35.3[3d^{10}]$
As	$7.83[4p^3]$	$17.6[4s^2]$	$26.9[3d^{10}]$

This appears in RIA scattering rate plots as steps located at the binding energies of the shells (see, e.g., Fig. 1). In our numerical analysis, we use the Compton profiles listed in Ref. [19] together with the atomic binding energies computed by cFAC [20], which we list in Table I.

The approach described in this section is widely used for Compton scattering calculations for electron recoil energies of $\mathcal{O}(\text{keV})$, but it becomes inaccurate for lower energies, as it fails to incorporate band-structure effects and the full response of the material. We discuss how to include these effects in the next section.

III. DIELECTRIC RESPONSE

We now present our new approach to computing the differential Compton scattering cross section, utilizing the material response of any target material.

The interaction Hamiltonian describing the nonrelativistic electron-photon interaction is given by

$$V_I = \frac{e}{m} \sum_a \vec{p}_a \cdot \vec{A}(\vec{x}_a, t) + \frac{e^2}{2m} \sum_a |\vec{A}(\vec{x}_a, t)|^2. \quad (9)$$

For the systems we consider, the bound electrons are nonrelativistic, and the terms proportional to A^2 dominate the interaction since $p_a/m \ll 1$. Therefore, we adopt the so-called A^2 approximation,

$$V_I = \frac{e^2}{2m} \sum_a |\vec{A}(\vec{x}_a, t)|^2. \quad (10)$$

Using Fermi's golden rule, the differential cross section for Compton scattering in the material is

$$\frac{d\sigma_{i \to f}}{d\Omega' d\omega'} = \frac{\omega'^2}{(2\pi)^3} |\langle \vec{p}_f, \lambda_f, S_f | V_I | \vec{p}_i, \lambda_i, S_i \rangle|^2$$
$$\times (2\pi)\delta(E_f + \omega' - E_i - \omega). \quad (11)$$

Here, S_i and S_f represent the initial and final states of the target material, and λ_i and λ_f represent the initial and final polarization states of the photon. The interaction matrix can be factored such that

$$\langle \vec{p}_f, \lambda_f, S_f | V_I | \vec{p}_i, \lambda_i, S_i \rangle = \frac{e^2}{2m\sqrt{\omega'\omega}} (\vec{\epsilon}_{\lambda_i,\vec{p}_i} \cdot \vec{\epsilon}^*_{\lambda_f,\vec{p}_f})$$
$$\times \sum_a \langle S_f | e^{i(\vec{p}_i - \vec{p}_f) \cdot \vec{x}} | S_i \rangle. \quad (12)$$

Averaging (summing) over the initial (final) photon polarizations, we can make the replacement $|\vec{\epsilon}_{\lambda_i,\vec{p}_i} \cdot \vec{\epsilon}^*_{\lambda_f,\vec{p}_f}|^2 \to (1 + \cos^2\theta)/2$. Summing over all final states of the material and averaging over the direction of the momentum transfers, we can write the differential cross section in the form

$$\frac{d\sigma_\omega}{d\Omega' d\omega' d(\Delta E)} = \frac{N_{\text{cell}} \alpha^2 \omega'}{2m^2 \omega} (1 + \cos^2\theta)$$
$$\times \delta(\Delta E + \omega' - \omega) \frac{df}{d(\Delta E)}, \quad (13)$$

where

$$\frac{df}{d(\Delta E)} = \frac{1}{N_{\text{cell}}} \sum_f \delta(E_f - E_i - \Delta E) \int \frac{d\Omega_{\hat{q}}}{4\pi} |\langle S_f | e^{i\vec{q}\cdot\vec{x}} | S_i \rangle|^2. \quad (14)$$

Here, $\vec{q} = \hat{q}q = \vec{p}_i - \vec{p}_f$ is the momentum transferred from the incoming photon to the detector target material, $\Omega_{\hat{q}}$ is the solid angle in the direction of $\vec{q}$, and N_{cell} is the number of unit cells in the crystal.

The above can be directly related to the dynamic structure factor at zero temperature $S(\Delta E, \vec{q})$, defined as [26]

$$S(\Delta E, \vec{q}) = \frac{2\pi}{V} \sum_f \delta(E_f - E_i - \Delta E) |\langle S_f | e^{i\vec{q}\cdot\vec{x}} | S_i \rangle|^2, \quad (15)$$

so

$$\frac{df}{d(\Delta E)} = \frac{V_{\text{cell}}}{2\pi} \int \frac{d\Omega_{\hat{q}}}{4\pi} S(\Delta E, \vec{q}). \quad (16)$$

Here, V is the volume of the target material, and $V_{\text{cell}} \equiv V/N_{\text{cell}}$ is the volume of the unit cell. The structure factor is equivalently written in terms of the dielectric function $\epsilon(\Delta E, \vec{q})$ as [26]

$$S(\Delta E, \vec{q}) = \frac{q^2}{2\pi\alpha} \text{Im}\left\{ \frac{-1}{\epsilon(\Delta E, \vec{q})} \right\}, \quad (17)$$

so Eq. (14) becomes

$$\frac{df}{d(\Delta E)} = \frac{q^2 V_{\text{cell}}}{4\pi^2 \alpha} \text{Im}\left\{ \frac{-1}{\epsilon(\Delta E, q)} \right\}. \quad (18)$$

Here, $\epsilon(\Delta E, q)$ is defined as the directional average of $\epsilon(\Delta E, \vec{q})$.[1]

Rewriting the solid angle Ω' in terms of the momentum transfer q and integrating over the final photon energy ω' in Eq. (13), we arrive at the differential Compton cross section per unit cell in terms of the dielectric function of the material,

$$\frac{d\sigma_\omega}{d(d\Delta E)dq} = \frac{\alpha V_{\text{cell}}}{4\pi m^2} \frac{q^3}{\omega^2} (1 + \cos^2\theta) \text{Im}\left(\frac{-1}{\epsilon(\Delta E, q)}\right). \quad (19)$$

The above equation is the main result of this paper, which we will use to compute the Compton scattering rates in various target materials relevant for sub-GeV DM searches. Below, we will present our results using an analytical approximation for the dielectric function, as well as using numerical tools.

The analytical approximation to the dielectric function that we use in this work is the Lindhard dielectric function [21,28], given by

$$\epsilon_{\text{Lind}} = 1 + \frac{3\omega_p^2}{q^2 v_F^2} \left(\frac{1}{2} + F_+ + F_-\right), \quad (20)$$

where

$$F_\pm = \frac{k_F}{4q} (1 - Q_\pm^2) \log^{\text{PV}} \frac{Q_\pm + 1}{Q_\pm - 1}, \quad (21)$$

$$Q_\pm = \frac{q}{2k_F} \pm \frac{m_e}{qk_F}(\omega + i\Gamma_p). \quad (22)$$

Here, $\omega_p = \sqrt{(4\pi\alpha n_e)/m_e}$ is the plasma frequency, and $k_F = (3\pi^2 n_e)^{1/3}$ is the Fermi momentum. For the width of the plasmon peak, Γ_p, we adopt 10% of the plasmon peak frequency.

We also employ several numerical methods to compute the dielectric function. We use the GPAW calculation with the local field effects (LFEs) dielectric function from DarkELF [21,22], and the valence-to-conduction-only dielectric function from EXCEED-DM [25,29].

Alternatively, we can employ a single-electron excitation approximation, where the photon excites an electron from the occupied to unoccupied bands (see Appendix A for more details). However, in reality, the low-energy excited

---

[1]The directional average of $\text{Im}\{-1/\epsilon(\Delta E, \vec{q})\}$ is well-approximated by taking the directional average over $\epsilon(\Delta E, \vec{q})$ for large $q \gg k_F$ where k_F is the Fermi momentum of the crystal, as the electron loss function $\text{Im}\{-1/\epsilon(\Delta E, \vec{q})\} \approx \text{Im}\{\epsilon(\Delta E, \vec{q})\}$ because $\text{Re}\{\epsilon(\Delta E, \vec{q})\} \approx 1$ and $\text{Im}\{\epsilon(\Delta E, \vec{q})\} \ll 1$. Further, Section III of Ref. [27] shows that the directional average of $\epsilon(\Delta E, \vec{q})$ produces results that are consistent with electron energy loss spectra, which also employs the energy loss function $\text{Im}\{1/\epsilon(\Delta E, \vec{q})\}$ and is dominated by low momentum transfer $q \lesssim k_F$.
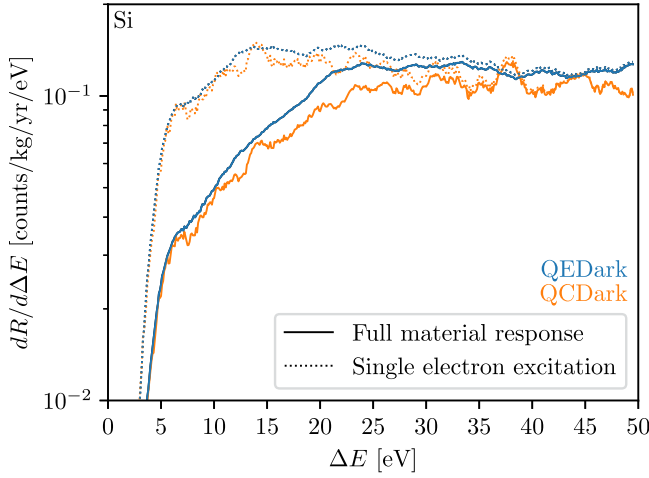
FIG. 2. Material response. We show the effect of the collective behavior of electrons in the context of Compton scattering rates in Si for incoming photons with $E_\gamma = 1.461$ MeV and $n_\gamma = 1.25 \times 10^{-14}$ cm^{-3}. The dashed lines only include the single-electron excitations that are captured by the imaginary part of the dielectric function, while the solid lines include the full material response, which differs from the former by a factor of $1/|\epsilon(\Delta E, q)|^2$. In constructing the full material response, we include the real part of $\epsilon(\Delta E, q)$ from the Lindhard dielectric function, Eq. (20).

states have very short lifetimes and deexcite by emitting low-energy photons, which are then immediately absorbed by the material. The correct out-states are thus dressed by the sum of such self-energy diagrams, which results in the factor of $1/|\epsilon(\Delta E, q)|^2$. Thus, the single-electron excitation approximation generally misses this factor in the target material response, including for Compton scattering and DM-electron scattering. We show the effects of omission of these collective effects in the context of Compton scattering in Fig. 2.

The single-electron excitation response is generally computed in terms of the crystal form factor [21,23,24],

$$|f_{\text{crystal}}(q, \Delta E)|^2 = \frac{q^5 V_{\text{cell}}}{8\pi^2 m^2 \alpha^2} \text{Im}(\epsilon_{\text{RPA}}(q, \Delta E)), \quad (23)$$

where $\epsilon_{\text{RPA}}(\Delta E, q)$ is the dielectric function calculated using the random phase approximation (RPA) [30–33]. We use QEDark [23] and QCDark [24] to compute the crystal form factor as additional numerical methods to obtain the material response. In order to accommodate the full response of the material, which also requires the real part of the dielectric function, we supplement our QEDark and QCDark calculations of the crystal form factor with the real part of the Lindhard dielectric function, Eq. (20). We use the Perdew-Burke-Ernzerhof (PBE) functional [34] with an $8 \times 8 \times 8$ **k** grid for all calculations for QEDark. To obtain the QCDark derived form factor, we use a PBE functional [34] for Si and a PBE0 [35] functional for Ge, both with a $6 \times 6 \times 6$ **k** grid.

IV. RESULTS

We are now in a position to compute Compton rates and compare our new approach that includes the dielectric material response to computations using RIA, FEFF, and single-electron excitations. In what follows, we present results for Si, Ge, GaAs, and SiC (3C), but our calculations can easily be extended to other materials.

Figure 1 shows the Compton scattering rates for a 1 kg · yr exposure in various crystals: Si (top-left panel), Ge (top-right panel), GaAs (bottom-left panel), and SiC (3C) (bottom-right panel), calculated using

$$\frac{dR}{d\Delta E} = n_\gamma \frac{M_{\text{Target}}}{M_{\text{cell}}} \frac{d\sigma_\omega}{d\Delta E}, \quad (24)$$

where M_{Target} and M_{cell} are the mass of the target material and the unit cell, respectively. We assume monochromic photons with energy $E_\gamma = 1.461$ MeV and a density of $n_\gamma = 1.25 \times 10^{-14}$ cm^{-3}, which corresponds to an ionization background of 1 event/kg/day/keV (commonly called "DRU") at energies of 1 keV in Si. Our calculation predicts a factor of roughly 0.33 fewer events/kg/yr in Si for $Q \le 5e^-$ compared to the prediction using RIA, where Q is the ionized charge defined in [36]. Our calculation also predicts a much smoother spectrum.

For Si and SiC, we find that all methods including the analytical Lindhard model (see Appendix C) produce consistent results, except RIA. The consistency between methods that do not include all-electron effects (such as DarkELF, QEDark, and the Lindhard model) with methods that include all-electron effects (such as EXCEED-DM and QCDark) implies that all-electron effects are not important for Compton scattering.[2]

On the other hand, because the Lindhard approximation and DarkELF (GPAW) [21,22] do not include information about the 3d shell in Ga, Ge, and As, they underestimate the Compton scattering cross section at higher recoil energies in Ge and GaAs target materials. Further, the usage of the hybrid PBE0 functional in the QCDark calculation for Ge affects the energy of the 3d shell compared to the PBE functional used in QEDark (for more details, see Ref. [24]). The energy obtained for the 3d shell using PBE0 lies between 28.6 eV and 29.0 eV, which is in close agreement with the experimental values of ∼29.5 eV [37].

As previously discussed, the QEDark and QCDark curves in all panels of Fig. 1 use the dielectric formalism, Eq. (19), where we use Eq. (23) to calculate the imaginary part of the dielectric function and the real part of the Lindhard dielectric function, Eq. (20). This enables one to more accurately encompass the many-body effects of the material response. We show these effects in Fig. 2 for a Si crystal,

---

[2]All-electron effects are important for DM-electron scattering for electron recoil energies $\gtrsim 20$ eV. We discuss the difference with Compton scattering further in Appendix C.
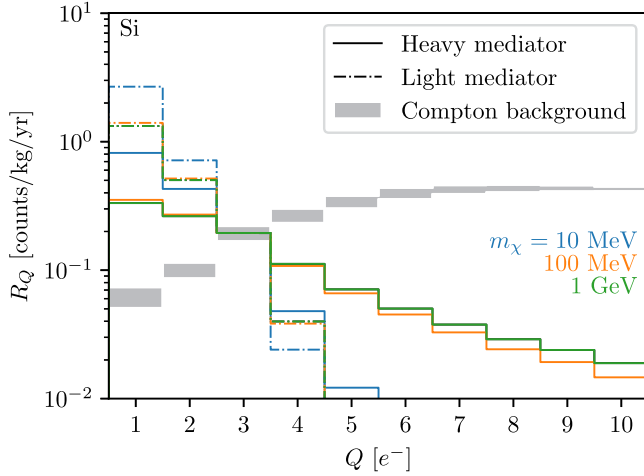
FIG. 3. Rates as a function of charge for Si. We show a comparison of the Compton scattering rates (gray bands) as a function of the charge ionized Q in a Si crystal with a background rate of 1 DRU at $\Delta E = 1$ keV using RIA. The lines show the DM-electron scattering rates computed with QCDark [24] for DM-electron cross sections listed in Table II. We use the secondary ionization model at 100 K from Ref. [36].

where the dashed lines include only the single-electron excitations that are captured by the imaginary part of the dielectric function, while the solid lines also include the real part of the Lindhard dielectric function to better capture the collective effects via the $1/|\epsilon(\Delta E, q)|^2$ factor. As we can see, collective effects in crystals reduce the Compton scattering cross sections at low energies $\lesssim 25$ eV by about a factor of ~ 3.

Figure 3 shows the expected Compton scattering rates for Si in terms of ionized charge following the secondary ionization modeling of Ref. [36]. The gray regions show the Compton scattering rates normalized to 1 DRU at $\Delta E = 1$ keV using RIA. The regions encompass the highest and lowest Compton scattering rates calculated using the Lindhard model, Eq. (20), and using DarkELF [21,22], EXCEED-DM [25,29], QEDark [23], and QCDark [24]. The various colored lines show, for comparison, the DM-electron scattering rates for different DM masses m_χ computed using QCDark. We normalize the DM-electron scattering cross sections to be equal to the Compton scattering cross section in the $Q = 3e^-$ bin. Table II lists

TABLE II. DM mass and DM-electron scattering cross section benchmarks for DM at reference momentum transfer $q = \alpha m_e$ used in the DM-electron scattering rates shown in Fig. 3.

m_χ	$\bar{\sigma}_e$ [cm²]	
	Light mediator	Heavy mediator
10 MeV	2.20×10^{-41}	1.71×10^{-42}
100 MeV	8.41×10^{-41}	4.82×10^{-42}
1 GeV	7.75×10^{-40}	4.42×10^{-41}
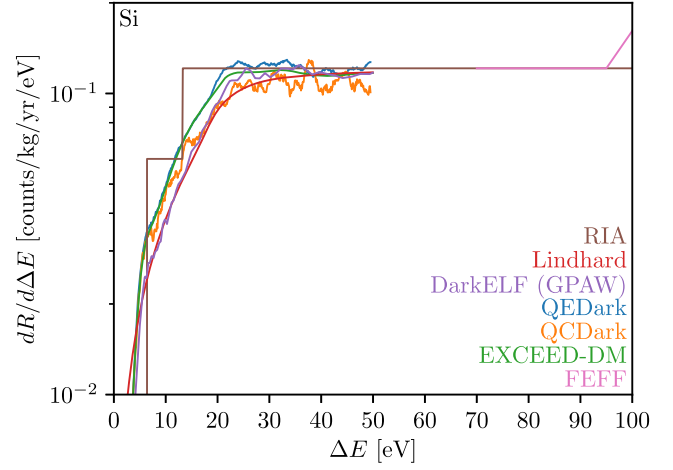
FIG. 4. Spotlight on Si. We give a reproduction of the top-left panel of Fig. 1 for Si with the energy axis extended to 100 eV. We see that our results match onto those computed with RIA and FEFF at high energies.

the derived cross sections. We note that the Compton spectrum decreases towards lower electron recoil energies, unlike the DM recoil spectra, which increase.

Figure 4 shows the expected Compton rates in Si for energies up to 100 eV, which indicates how our results match with those obtained using the FEFF code [6–9]. The results from the FEFF code were recently compared to experimental data by the DAMIC-M Collaboration and found to be roughly consistent at energies $\Delta E \gtrsim \mathcal{O}(100$ eV$)$ [10].

V. SUMMARY

In this paper, we have proposed a rigorous way to compute Compton scattering rates utilizing the material response of the target. This is particularly useful in the low-energy regime. We show how the dielectric function of any material can be used to precisely evaluate the Compton scattering cross section near the energy thresholds. The dielectric function approach is convenient as it incorporates the many-body effects of the system, including all-electron and band-structure effects. The Compton scattering rate can then be calculated using existing codes, analytical forms, or experimental data. Importantly, we find that the simple analytical Lindhard function often captures well the behavior of the Compton scattering rate over a broad range of materials, allowing one to swiftly and accurately obtain the Compton rate.

As a concrete example, we calculated the event rate for Si, Ge, GaAs, and SiC with various methods. Compared with the conventional RIA method, our new approach, which includes band-structure effects, leads to smoother Compton scattering cross sections for energies below several 10's of eV. It is necessary to include collective effects of the electron density, which lowers the Compton

scattering rates for energies below ~ 25 eV. The all-electron corrections are found to be small for Compton scattering.

APPENDIX A: SINGLE-ELECTRON EXCITATIONS IN CRYSTALS

In general, the cross section for a $2 \to 2$ process is

$$\sigma_{\vec{p}, \vec{k}} = \frac{1}{16 E_p E_k v_{\text{rel}}} \int \frac{d^3 q}{(2\pi)^3} \frac{d^3 k'}{(2\pi)^3} \frac{\overline{|\mathcal{M}|^2}}{E_{|\vec{p}-\vec{q}|} E_{k'}}$$
$$\times (2\pi)^4 \delta(E_i - E_f) \delta^3(\vec{k} + \vec{q} - \vec{k'}), \quad \text{(A1)}$$

where the integration is over the final momenta of the two particles, v_{rel} is the initial relative speed of the particles, and $\mathcal{M}$ is the amplitude that describes the interaction. For Compton scattering, $\vec{k}$ and $\vec{k'}$ are the initial and final momenta of the electron, and $\vec{p}$ and $\vec{p'} = \vec{p} - \vec{q}$ are the initial and final momenta of the photon. Here, E_i and E_f are the total initial and final energies of the system. A bound electron in the detector will have a nonrelativistic momentum, so $v_{\text{rel}} \approx 1$.

We now follow a similar approach to Ref. [23]. The nonrelativistic amplitude in free-electron Compton scattering is defined by

$$\langle \gamma_{\vec{p}-\vec{q}}, e_{\vec{k'}} | H_{\text{int}} | \gamma_{\vec{p}}, e_{\vec{k}} \rangle = C \mathcal{M}_{\text{free}} (2\pi)^3 \delta^3(\vec{k} + \vec{q} - \vec{k'}), \quad \text{(A2)}$$

where C is an unimportant constant. For a bound electron in a detector, its state can be represented by a superposition of plane waves, $|e\rangle = \sqrt{V} \int \frac{d^3 k}{(2\pi)^3} \tilde{\psi}(\vec{k}) |e_{\vec{k}}\rangle$, so the overlap integral can be written as

$$\langle \gamma_{\vec{p}-\vec{q}}, e_f | H_{\text{int}} | \gamma_{\vec{p}}, e_i \rangle = V \int \frac{d^3 k}{(2\pi)^3} \tilde{\psi}_i(\vec{k}) \tilde{\psi}_f^*(\vec{k} + \vec{q}) C \mathcal{M}_{\text{free}}. \quad \text{(A3)}$$

In general, $\mathcal{M}_{\text{free}}$ depends on the initial momentum of the electron and, therefore, cannot be pulled out of the integral. However, assuming the electron is nonrelativistic before and after the collision, which is consistent with energy transfers in the range $\lesssim 50$ eV, our amplitude reduces to that of Thomson scattering [15],

$$\overline{|\mathcal{M}_{\text{free}}|^2} = 2e^4 \left[\frac{k \cdot p'}{k \cdot p} + \frac{k \cdot p}{k \cdot p'} + 2m^2 \left(\frac{1}{k \cdot p} - \frac{1}{k \cdot p'} \right) \right.$$
$$\left. + m^4 \left(\frac{1}{k \cdot p} - \frac{1}{k \cdot p'} \right)^2 \right] \quad \text{(A4)}$$

$$\approx 2e^4 (1 + \cos^2 \theta). \quad \text{(A5)}$$

The Thomson scattering amplitude does not depend on the initial momenta of the electron, so it can be factored out of the integral in Eq. (A3). By squaring Eqs. (A2) and (A3) and comparing them, we see that going from a free electron to a bound electron amounts to the following substitution,

$$(2\pi)^3 \overline{|\mathcal{M}_{\text{free}}|^2} V \delta^3(\vec{k} + \vec{q} - \vec{k'}) \to V^2 \overline{|\mathcal{M}_{\text{free}}|^2} |f_{i \to f}(\vec{q})|^2, \quad \text{(A6)}$$

where $f_{i \to f}(\vec{q})$ is the atomic form factor defined as

$$f_{i \to f}(\vec{q}) = \int d^3 x \, \psi_i(\vec{x}) \psi_f^*(\vec{x}) e^{i \vec{q} \cdot \vec{x}}. \quad \text{(A7)}$$

The factor of V on the left of Eq. (A6) is due to the redundant delta function after squaring, which contributes a factor of $\frac{V}{(2\pi)^3}$. Applying this substitution in Eq. (A1), considering only a single final electron state, and letting E and E' (ω and ω') be the initial and final energies of the electron (photon), we find

$$\sigma_{\vec{p}, e_i \to e_f} = \frac{1}{4 E \omega} \int \frac{d^3 q}{(2\pi)^3} \frac{1}{4 E' \omega'} (2\pi) \delta(E_i - E_f)$$
$$\times \overline{|\mathcal{M}_{\text{free}}|^2} |f_{i \to f}(\vec{q})|^2. \quad \text{(A8)}$$

The initial and final energies of the system are

$$E_i = \omega + m + E_{e,i} \quad \text{(A9)}$$

and

$$E_f = \omega' + m + E_{e,f}$$
$$= \sqrt{\omega^2 + q^2 - 2\omega q \cos\theta_{pq}} + m + E_{e,f}, \quad (A10)$$

where $E_{e,i}$ and $E_{e,f}$ are the initial and final energies of the electron excluding the rest mass of the electron, i.e., $E_{e,i} = E - m$ and $E_{e,f} = E' - m$. We can eliminate the delta function by averaging over initial photon momenta directions. We assume a spherically symmetric distribution of incident photons, and we take $E, E' \approx m$ since the electron is nonrelativistic before and after scattering, which gives

$$\sigma_{\omega,e_i \to e_f} = \frac{1}{128\pi^2 m^2 \omega^2} \int d^3 q \frac{1}{q} \overline{|\mathcal{M}_{\text{free}}|^2} |f_{i \to f}(\vec{q})|^2. \quad (A11)$$

We obtain the kinematic constraints $\Delta E \le q \le 2\omega - \Delta E$ and $\Delta E \le \omega$, where $\Delta E = E_{e,f} - E_{e,i}$.

For electrons in a periodic lattice, by Bloch's theorem, the electronic wave functions are described by a plane wave modulated by a periodic function,

$$\psi_{i,\vec{k}}(\vec{x}) = \frac{1}{\sqrt{V}} \sum_{\vec{G}} u_i(\vec{k} + \vec{G}) e^{i(\vec{k}+\vec{G})\cdot\vec{x}}, \quad (A12)$$

where $\vec{k}$ is a wave vector in the first Brillouin zone, $\vec{G}$ is the reciprocal lattice vector, and the subscript i is the band index. The wave functions are normalized such that $\sum_{\vec{G}} |u_i(\vec{k} + \vec{G})|^2 = 1$.

Substituting Eq. (A12) into Eq. (A7) and squaring yields

$$|f_{i,\vec{k} \to i',\vec{k}'}|^2 = \sum_{\vec{G}'} (2\pi)^3 \delta^{(3)}(\vec{q} - (\vec{k}' + \vec{G}' - \vec{k})) \frac{1}{V} |f_{[i\vec{k},i'\vec{k}',\vec{G}']}|^2,$$
$$(A13)$$

where

$$f_{[i\vec{k},i'\vec{k}',\vec{G}']} = \sum_{\vec{G}} u_{i'}^*(\vec{k}' + \vec{G} + \vec{G}') u_i(\vec{k} + \vec{G}). \quad (A14)$$

We have replaced the subscripts $i \to f$ with the more explicit $i, \vec{k} \to i', \vec{k}'$. Then, our cross section becomes

$$\sigma_{\omega,\{i,\vec{k}\} \to \{i',\vec{k}'\}} = \frac{\pi}{16m^2\omega^2} \frac{1}{q} \overline{|\mathcal{M}_{\text{free}}|^2}$$
$$\times \sum_{\vec{G}'} \frac{1}{V} |f_{[i\vec{k},i'\vec{k}',\vec{G}']}|^2 \Big|_{q=|\vec{k}'+\vec{G}'-\vec{k}|}. \quad (A15)$$

Summing over all initial and final electron states and multiplying by 2 to account for the two degenerate spin states gives the total scattering cross section from the crystal,

$$\sigma_\omega = \frac{\pi}{8m^2\omega^2} V_{\text{cell}} N_{\text{cell}} \sum_{ii'} \int_{\text{BZ}} \frac{d^3 k d^3 k'}{(2\pi)^6} \frac{1}{q} \overline{|\mathcal{M}_{\text{free}}|^2}$$
$$\times \sum_{\vec{G}'} |f_{[i\vec{k},i'\vec{k}',\vec{G}']}|^2 \Big|_{q=|\vec{k}'+\vec{G}'-\vec{k}|}. \quad (A16)$$

Here, N_{cell} and V_{cell} are the number of atoms in the primitive cell and the volume of the primitive cell, and the integral is over the first Brillouin zone in the crystal's reciprocal space. To obtain the differential cross section, we integrate over delta functions, leaving

$$\frac{d\sigma_\omega}{d(\Delta E)dq} = \frac{\alpha N_{\text{cell}}}{16\pi\omega^2} \frac{1}{q^2} \overline{|\mathcal{M}_{\text{free}}|^2} |f_{\text{crystal}}(q, \Delta E)|^2, \quad (A17)$$

where $f_{\text{crystal}}(q, \Delta E)$ is the crystal form factor [23],

$$|f_{\text{crystal}}(q, \Delta E)|^2 = \frac{2\pi^2}{\alpha m^2 V_{\text{cell}}} \sum_{ii'} \int_{\text{BZ}} V_{\text{cell}}^2 \frac{d^3 k d^3 k'}{(2\pi)^6}$$
$$\times \delta(\Delta E - E_{i',\vec{k}'} + E_{i,\vec{k}})$$
$$\times \sum_{\vec{G}'} q\delta(q - |\vec{k}' - \vec{k} + \vec{G}'|)$$
$$\times |f_{[i\vec{k},i'\vec{k}',\vec{G}']}|^2. \quad (A18)$$

Lastly, we substitute in the Thomson scattering amplitude and divide by the number of cells to get the differential cross section per unit cell,

$$\frac{d\sigma_\omega}{d(\Delta E)dq} = \frac{2\pi\alpha^3}{\omega^2} \frac{(1 + \cos^2\theta)}{q^2} |f_{\text{crystal}}(q, \Delta E)|^2. \quad (A19)$$

Using Eq. (23), we find that Eq. (A19) can be written as

$$\frac{\sigma_\omega}{d(d\Delta E)dq} = \frac{\alpha V_{\text{cell}}}{4\pi m^2} \frac{q^3}{\omega^2} (1 + \cos^2\theta) \text{Im}\{\epsilon(\Delta E, q)\}. \quad (A20)$$

Comparing to Eq. (19), we see that the single-electron excitation approach misses a factor of $1/|\epsilon(\Delta E, q)|^2$ and hence fails to capture the complete density response of the system as discussed in the main text. In effect, this approach misses the self-energy corrections to the photon in the target material.

APPENDIX B: DENSITY FUNCTIONAL THEORY

The dielectric function and the crystal form factor, as shown in Eqs. (19) and (23), depend on the electronic structure of the target material. Here, we provide a short review of density functional theory (DFT), which is the typical method used to approximate the orbital wave functions and energy levels [21–23,25,29]. DFT rests on two major theorems, known as the Hohenberg-Kohn theorems [38],

(1) The energy of the ground state is a unique functional of the electron density.
(2) The electron density that minimizes the energy is the correct solution to the ground state (variational theorem).

The energy functional, in terms of the electron density $n(\vec{r})$, is given by [39]

$$E[n] = T_{S}[n] + \int d^3 r v_{\text{ext}}(\vec{r}) n(\vec{r})$$
$$+ \frac{1}{2} \int d^3 r \int d^3 r' \frac{n(\vec{r}) n(\vec{r}')}{|\vec{r} - \vec{r}'|} + E_{\text{xc}}[n], \qquad \text{(B1)}$$

where T_S is the kinetic energy of noninteracting orbitals, $v_{\text{ext}}(\vec{r})$ is the external potential from the nuclei, and E_{xc}, known as the exchange and correlation functional, models the quantum interactions missing in T_S and the Hartree electron-electron interaction (third term).

The minimization of the energy functional with the constraint that the total number of electrons remains constant leads to the Kohn-Sham equations [39],

$$\left(-\frac{1}{2}\vec{\nabla}^2 + v_{\text{ext}}(\vec{r}) + \int \frac{n(\vec{r}')}{|\vec{r} - \vec{r}'|} d^3 r' + v_{\text{xc}}(\vec{r}) \right) \phi_i(\vec{r})$$
$$= \epsilon_i \phi_i(\vec{r}), \qquad \text{(B2)}$$

where ϵ_i and $\phi_i(\vec{r})$ are the energy levels and wave functions of the ith orbital, respectively, and

$$v_{\text{xc}}(\vec{r}) = \frac{\delta E_{\text{xc}}[n]}{\delta n(\vec{r})}. \qquad \text{(B3)}$$

Because the Hamiltonian depends on $n(\vec{r})$, which depends on the occupied orbitals $\{\phi_i(\vec{r})\}$, this equation must be solved self-consistently.

The exact form of the exchange and correlation functional is not known, though there are multiple models available. In this paper, we use the PBE functional [34] for both QEDark and QCDark in Si. For Ge, we use PBE and PBE0 [35] functionals in QEDark and QCDark, respectively. We use the standard available results for DarkELF [22] and the valence-to-conduction-band-only results for EXCEED-DM [25].

APPENDIX C: EFFECTIVENESS OF THE LINDHARD MODEL

The Lindhard model produces reliable results for the Compton scattering cross section for valence electrons and hence produces reliable results until the effects of core electrons become important. For example, for Si, the Lindhard model produces reliable results for $\Delta E \lesssim 99$ eV, while for Ge it produces reliable results for $\Delta E \lesssim 29.2$ eV.

The left panel of Fig. 5 shows the f-sum rule [40] for the loss function calculated for Si using various methods. We see that the Mermin model overestimates the electron loss function, $\text{Im}\{-1/\epsilon(\Delta E, q)\}$, for $q \gtrsim 12$ keV, and we further note that the Lindhard model underestimates the loss function at high $q \gtrsim 12$ keV.

The differential cross section for any general process, where an incoming particle with speed β relative to the target material transfers energy ΔE and momentum q to an electron, is

$$\frac{d\sigma}{d\Delta E} = \int_{q_{\text{min}}}^{\infty} dq \frac{\partial^2 \sigma}{\partial \Delta E \partial q}, \qquad \text{(C1)}$$

where $q_{\text{min}} = \Delta E / \beta$ is the minimum momentum transfer required to transfer energy ΔE. In the case of Compton
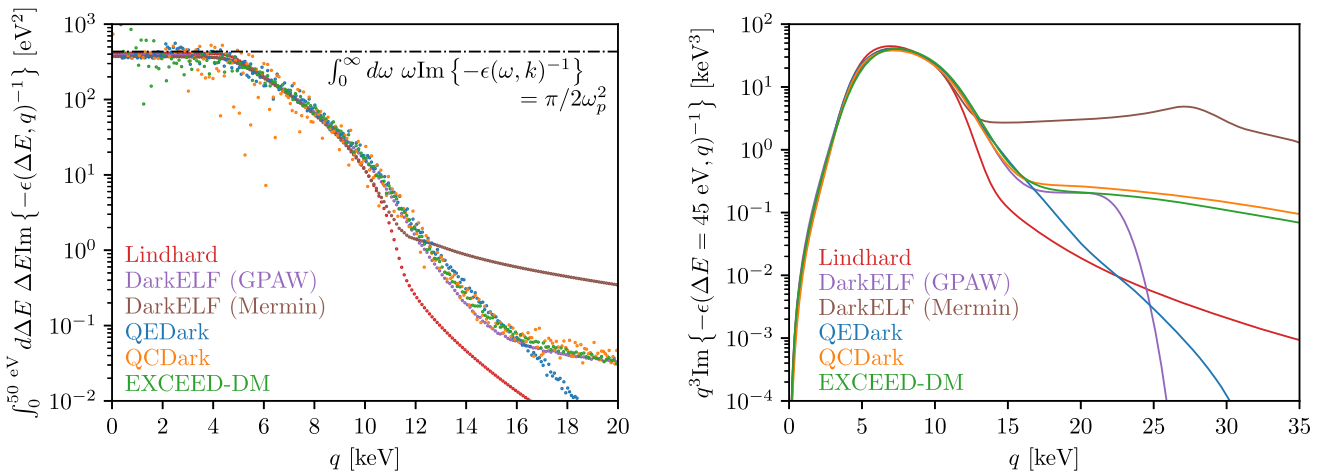
FIG. 5. Left panel: f-sum rule [40] for the loss function calculated for Si using various methods. Right panel: electron loss function $\text{Im}\{-\epsilon(\Delta E, q)^{-1}\}$ for Si, weighted by momenta factors relevant for Compton scattering, calculated at $\Delta E = 45$ eV. For this plot, we average the electron loss function over a 2 eV bin centered at 45 eV and apply a 1D Gaussian filter in k with $\sigma_k = 1$ keV. Note the presence of high-q modes due to all-electron modeling in QCDark and EXCEED-DM compared to DarkELF and QEDark.

scattering, the incoming particles are photons ($\beta = 1$), hence upon integrating Eq. (19) in q, one obtains

$$\frac{d\sigma_\omega}{d\Delta E} = \frac{\alpha V_{\text{cell}}}{4\pi m^2} \int_{\Delta E}^{\infty} dq \frac{q^3}{\omega^2} (1 + \cos^2\theta) \text{Im}\left(\frac{-1}{\epsilon(\Delta E, q)}\right). \quad \text{(C2)}$$

Hence, the peak in the electron loss function $\text{Im}\{-\epsilon(\Delta E, q)^{-1}\}$ dominates. This is demonstrated in the right panel of Fig. 5. The low-q region is captured well by the Lindhard model for valence electrons, and hence the

Lindhard model provides reliable Compton scattering rates in the low-energy regime.

This is in contrast to DM-electron scattering where the incoming DM particles have a speed $\beta \sim \mathcal{O}(10^{-3})$; thus, for $\Delta E \sim \mathcal{O}(10 \text{ eV})$, the lowest possible momentum transfer is $q_{\min} \sim \mathcal{O}(10 \text{ keV})$. Further, capturing the electron loss function at high momentum transfer makes inclusion of all-electron effects necessary [24,25,29]. The Lindhard response function of the material thus captures the Compton scattering rates well but does not capture the DM-electron scattering rates well [21,28].

[1] R. Essig *et al.*, Snowmass 2021 cosmic frontier: The landscape of low-threshold dark matter direct detection in the next decade, in *Snowmass 2021* (2022), arXiv:2203.08297.

[2] R. Essig, J. Mardon, and T. Volansky, Direct detection of sub-GeV dark matter, Phys. Rev. D **85**, 076007 (2012).

[3] S. Agostinelli *et al.* (GEANT4 Collaboration), Geant4—A simulation toolkit, Nucl. Instrum. Methods Phys. Res., Sect. A **506**, 250 (2003).

[4] J. Allison *et al.*, Geant4 developments and applications, IEEE Trans. Nucl. Sci. **53**, 270 (2006).

[5] J. Allison *et al.*, Recent developments in Geant4, Nucl. Instrum. Methods Phys. Res., Sect. A **835**, 186 (2016).

[6] J. J. Rehr and R. C. Albers, Theoretical approaches to x-ray absorption fine structure, Rev. Mod. Phys. **72**, 621 (2000).

[7] J. J. Rehr, J. J. Kas, M. P. Prange, A. P. Sorini, Y. Takimoto, and F. Vila, *Ab initio* theory and calculations of x-ray spectra, C. R. Phys. **10**, 548 (2009), theoretical spectroscopy.

[8] J. J. Rehr, J. J. Kas, F. D. Vila, M. P. Prange, and K. Jorissen, Parameter-free calculations of x-ray spectra with FEFF9, Phys. Chem. Chem. Phys. **12**, 5503 (2010).

[9] J. J. Kas, F. D. Vila, C. D. Pemmaraju, T. S. Tan, and J. J. Rehr, Advanced calculations of x-ray spectroscopies with FEFF10 and Corvus, J. Synchrotron Radiat. **28**, 1801 (2021).

[10] D. Norcini *et al.* (DAMIC-M Collaboration), Precision measurement of Compton scattering in silicon with a skipper CCD for dark matter detection, Phys. Rev. D **106**, 092001 (2022).

[11] J. Korringa, On the calculation of the energy of a Bloch wave in a metal, Physica (Amsterdam) **13**, 392 (1947).

[12] W. Kohn and N. Rostoker, Solution of the Schrödinger equation in periodic lattices with an application to metallic lithium, Phys. Rev. **94**, 1111 (1954).

[13] G. Fernandez-Moroni, R. Harnik, P. A. N. Machado, I. Martinez-Soler, Y. F. Perez-Gonzalez, D. Rodrigues, and S. Rosauro-Alcaraz, The physics potential of a reactor neutrino experiment with Skipper-CCDs: Searching for new physics with light mediators, J. High Energy Phys. 02 (2022) 127.

[14] A. M. Botti *et al.*, Constraints on the electron-hole pair creation energy and Fano factor below 150 eV from Compton scattering in a skipper CCD, Phys. Rev. D **106**, 072005 (2022).

[15] M. E. Peskin and D. V. Schroeder, *An Introduction to Quantum Field Theory* (Addison-Wesley, Reading, USA, 1995).

[16] R. Ribberfors, Relationship of the relativistic Compton cross section to the momentum distribution of bound electron states, Phys. Rev. B **12**, 2067 (1975).

[17] R. Ribberfors, Relationship of the relativistic Compton cross section to the momentum distribution of bound electron states. II. Effects of anisotropy and polarization, Phys. Rev. B **12**, 3136 (1975).

[18] D. Brusa, G. Stutz, J. Riveros, J. Fernández-Varea, and F. Salvat, Fast sampling algorithm for the simulation of photon Compton scattering, Nucl. Instrum. Methods Phys. Res., Sect. A **379**, 167 (1996).

[19] F. Biggs, L. Mendelsohn, and J. Mann, Hartree-Fock Compton profiles for the elements, At. Data Nucl. Data Tables **16**, 201 (1975).

[20] M. F. Gu, The flexible atomic code, Can. J. Phys. **86**, 675 (2008).

[21] S. Knapen, J. Kozaczuk, and T. Lin, Dark matter-electron scattering in dielectrics, Phys. Rev. D **104**, 015031 (2021).

[22] S. Knapen, J. Kozaczuk, and T. Lin, Python package for dark matter scattering in dielectric targets, Phys. Rev. D **105**, 015014 (2022).

[23] R. Essig, M. Fernandez-Serra, J. Mardon, A. Soto, T. Volansky, and T.-T. Yu, Direct detection of sub-GeV dark matter with semiconductor targets, J. High Energy Phys. 05 (2016) 046.

[24] C. E. Dreyer, R. Essig, M. Fernandez-Serra, A. Singal, and C. Zhen, Fully *ab-initio* all-electron calculation of dark matter–electron scattering in crystals with evaluation of systematic uncertainties, arXiv:2306.14944.

[25] T. Trickle, Extended calculation of electronic excitations for direct detection of dark matter, Phys. Rev. D **107**, 035035 (2023).

[26] K. Sturm, Dynamic structure factor: An introduction, Z. Naturforsch. A **48**, 233 (1993).

[27] R. Essig, R. Plestid, and A. Singal, Collective excitations and low-energy ionization signatures of relativistic particles in silicon detectors, arXiv:2403.00123.

[28] Y. Hochberg, Y. Kahn, N. Kurinsky, B. V. Lehmann, T. C. Yu, and K. K. Berggren, Determining dark-matter–electron scattering rates from the dielectric function, Phys. Rev. Lett. **127,** 151802 (2021).

[29] S. M. Griffin, K. Inzani, T. Trickle, Z. Zhang, and K. M. Zurek, Extended calculation of dark matter-electron scattering in crystal targets, Phys. Rev. D **104,** 095015 (2021).

[30] D. Bohm and D. Pines, A collective description of electron interactions. I. Magnetic interactions, Phys. Rev. **82,** 625 (1951).

[31] D. Pines and D. Bohm, A collective description of electron interactions: II. Collective vs individual particle aspects of the interactions, Phys. Rev. **85,** 338 (1952).

[32] D. Bohm and D. Pines, A collective description of electron interactions: III. Coulomb interactions in a degenerate electron gas, Phys. Rev. **92,** 609 (1953).

[33] H. Ehrenreich and M. H. Cohen, Self-consistent field approach to the many-electron problem, Phys. Rev. **115,** 786 (1959).

[34] J. P. Perdew, K. Burke, and M. Ernzerhof, Generalized gradient approximation made simple, Phys. Rev. Lett. **77,** 3865 (1996).

[35] C. Adamo and V. Barone, Toward reliable density functional methods without adjustable parameters: The PBE0 model, J. Chem. Phys. **110,** 6158 (1999).

[36] K. Ramanathan and N. Kurinsky, Ionization yield in silicon for eV-scale electron-recoil processes, Phys. Rev. D **102,** 063026 (2020).

[37] J. A. Bearden and A. F. Burr, Reevaluation of x-ray atomic energy levels, Rev. Mod. Phys. **39,** 125 (1967).

[38] P. Hohenberg and W. Kohn, Inhomogeneous electron gas, Phys. Rev. **136,** B864 (1964).

[39] W. Kohn and L. J. Sham, Self-consistent equations including exchange and correlation effects, Phys. Rev. **140,** A1133 (1965).

[40] F. Bassani, Optical sum rules and Kramers–Kronig relations, in *Encyclopedia of Condensed Matter Physics*, edited by F. Bassani, G. L. Liedl, and P. Wyder (Elsevier, Oxford, 2005), pp. 200–206.